Title

An Ultrasensitive Molecular Detector for Direct Sensing of Spin Currents at Room Temperature

Author

Feggeler, Thomas

Publication Date

2024-09-24

An ultrasensitive molecular detector for direct sensing of spin currents at room temperature

Thomas Feggeler[1,2]*, Ralf Meckenstock*[3]*, Tanja Strusch*[3]*, Maria V. Efremova*[4]*, Michael Farle*[3]
and Ulf Wiedwald[3]*

[1]Department of Physics, University of California, Berkeley, Berkeley, CA-94720, United States

[2]Advanced Light Source, Lawrence Berkeley National Laboratory, Berkeley, CA-94720, United States

[3]Faculty of Physics and Center for Nanointegration Duisburg-Essen (CENIDE), University of Duisburg-Essen, Germany

[4]Department of Applied Physics and Science Education, Eindhoven University of Technology, Eindhoven, 5600 MB, The Netherlands

*corresponding author: ulf.wiedwald@uni-due.de

KEYWORDS

Spin current, Sensor, Electron paramagnetic resonance, Oleic acid, Magnetic Nanoparticles

ABSTRACT

The experimental analysis of pure spin currents at interfaces is one major goal in the field of magnonics and spintronics. Complimentary to the established Spin-Hall effect using the spin-to-charge conversion in heavy metals for information processing, we present a novel approach based on spin pumping detection by an interfacial, resonantly excited molecular paramagnet adsorbed to the surface of the spin current generating magnet. Here, we show that the sensitivity of this electron paramagnetic resonance (EPR) detector can be enhanced by orders of magnitude through intramolecular transfer of spin polarization at room temperature. Our proof-of-principle sample consists of octahedral-shaped ferrimagnetic Fe_3O_4 nanoparticles covered by oleic acid (OA) which has two paramagnetic centers, S1 and S2. S1 arises from the chemisorption of OA and is located directly at the interface to Fe_3O_4. S2 originates from radical formation at the center of the molecule close to the double bond of oleic acid and is not influenced by chemisorption. Using ferromagnetic resonance (FMR) excitation of the Fe_3O_4 nanoparticles to pump spins into S1, a population inversion of the spin-split levels of S2 is formed, vastly enhancing the detection sensitivity on the atomic scale.

1. INTRODUCTION

Contemporary silicon-based computing is limited by its energy consumption,[1] and further progress -towards faster and energy-efficient (green) computing needs new concepts. Spintronics is the most promising technology to overcome these limits.[2] In this field, the spin of an electron and its charge-free currents, i.e., pure spin currents and low energy magnons, are the information carriers representing the ultimate goal for data processing at low power.[3-5] An established technique to detect spin currents is the inverse Spin-Hall effect, which converts a spin current into an electric voltage using bi-layers consisting of a ferromagnetic and a metallic layer with large spin-orbit coupling (Pt, W or Ta for example)[6-9]. This approach requires the layers to be electrically conductive and contacted, which is difficult to integrate in nanoscale devices.

An alternative method to probe pure spin currents are paramagnetic molecular markers which do not require electrical contacts and provide a signal for remote sensing.[10] We suggest a concept for an ultra-sensitive, non-destructive spin current detection on the few-nm scale employing transfer of spin polarization on the molecular level. Such a detection scheme is based on electron paramagnetic resonance (EPR) as demonstrated below. The population inversion in a two-level system has been suggested for tremendously enhancing the sensitivity for the detection of EPR.[11] Historically, such concepts have found applications in astronomical observations[12,13], and ultrasensitive magnetic resonance spectroscopy.[11] Here, we exploit such a detector to realize a novel ultrasensitive molecular spin current sensor offering the high sensitivity required to detect spin currents in nanoscale systems, especially such as polyhedral nanoparticles.

The molecular detector is oleic acid (OA), which is widely used as a surfactant for the stabilization of nanoparticles in colloidal chemistry.[14, 15] After nanoparticle synthesis at high temperature, OA harbors two EPR centers, i.e. uncompensated spin moments. One is the chemical bond to the nanoparticle (referred to as S1 in the following) and the second is located close to the double bond in OA, roughly in the center of the carboxyl chain (S2 in the following).[16] By taking the magnetic stray field distribution at and near the surface of Fe_3O_4 nanoparticles quantitatively into account, we demonstrate that the nanoscale variation of magnetic stray fields around a nanoparticle increases the EPR linewidth of S1 such that the resonant coupling to S2 becomes possible, and the population inversion of S2 is achieved. This forms a delicate sensing scheme for small spin currents based on a single interfacial molecule.

1.1 Spin inversion detection scheme. The spin current detection system consisting of OA molecules chemisorbed on Fe_3O_4 octahedra is explained in the following. Figure 1 (a) shows a sketch of the design (not to scale) with an OA molecule at the surface of Fe_3O_4 facets. The principle of EPR is shown in Figure 1b. The spin degeneracy is lifted in a homogeneous magnetic field $\vec{B}_{ext}$ by the Zeeman effect. Microwaves with their magnetic component $\vec{B}_{MW}$ perpendicular to $\vec{B}_{ext}$ are absorbed if the resonance condition $hv = g\mu_B B_{res}$ is fulfilled.[17] Figure 1c shows the typical Lorentzian line shape at the resonance field $|\vec{B}_{ext}| = |\vec{B}_{res}| = \frac{\omega}{\gamma}$ with ω the angular frequency and γ the gyromagnetic ratio. It is important to note that the resonance linewidth ΔB of S1 and S2 differ by one order of magnitude. S1 exhibits the larger linewidth[10] ($\Delta B > 500\ \mu T$), and the one of S2 is much narrower[16] at $\Delta B < 60 \mu T$, respectively. Due to the different g-factors of S1[10]: $g = 2.004 \pm 0.001$ and S2: $g = 2.024 \pm 0.001$ (see Supplementary Information) and their linear dispersion in $\vec{B}_{ext}$, S1 and S2 EPR resonances never overlap (Figure 1d) in absence of additional field sources.

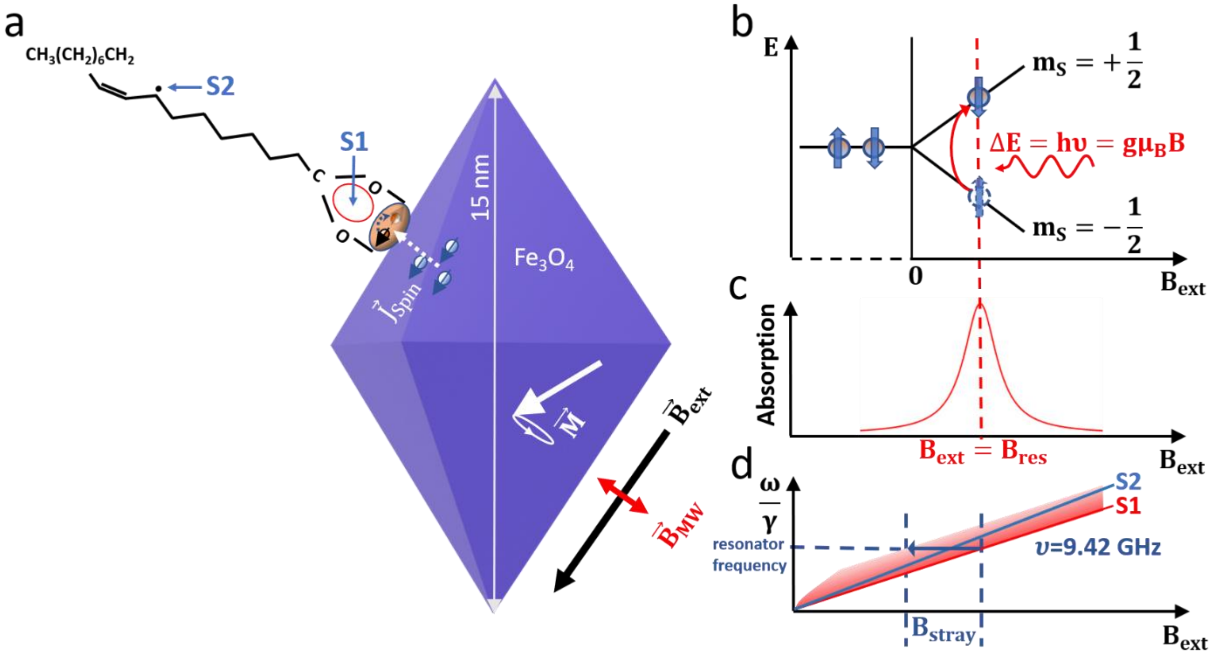

Figure 1. (a) Schematics of an octahedral Fe_3O_4 nanoparticle in a static magnetic field $\vec{B}_{ext}$ and microwave field $\vec{B}_{MW}$. The spin current $\vec{J}_{Spin}$ and the unpaired EPR center S1 at the interface are sketched. The molecular structure of OA is shown with the EPR center S2 located close to the double bond of the carboxyl chain (not to scale). (b) Principle of EPR: Zeeman splitting in an external magnetic field $\vec{B}_{ext}$. Resonant absorption is obtained in case the microwave photon energy ($h\upsilon = g\mu_B B_{res}$) equals the energy difference between spin-split states. (c) Microwave absorption as function of magnetic field: EPR resonance position B_{res}. (d) Dispersion relation of the EPR center S1 and S2 of OA. Due to the different g-factors, S1 and S2 states do not overlap energetically at $\vec{B}_{ext} > 0$. The inhomogeneous magnetic stray field $\vec{B}_{stray}(x, y, z)$ of Fe_3O_4 nanoparticles with a magnitude depending on the distance to the nanoparticle and $\vec{B}_{ext}$ form the local resonance field. For S1, this effect is indicated by the red-shaded area.

1.2 Stimulated amplification in the molecular detector. The resonance linewidth, intensity, and position of the two EPR centers, S1 and S2, are modified by the local stray field distribution of the nanoparticles yielding a broadening and overlap of the two resonance lines, thus making crosstalk possible. The EPR center S1, with its shorter intrinsic lifetime, relaxes into the upper level of center S2, which will finally lead to a stimulated emission of microwaves at S2 when driven out of equilibrium. Ideally, for this scheme to work, the resonance condition of EPR center S1 shall be modified without or only a small influence on S2. This is realized by the interfacial magnetic stray field B_{stray} of the nanoparticle, which adds a small magnetic field component to the effective resonance field B_{res}, as indicated by the red-shaded area in Figure 1d. On the other hand, the center S2 sits at a distance > 1 nm to the Fe_3O_4 surface. At this distance, the stray field of the particle is so large that the resonance conditions of S2 cannot be matched. The growing stray field is quantified by micromagnetic simulations (see Supplementary information, Figure S1). Thus, S2 is solely excited by S1 relaxations. Of note, the additional stray field component is always positive since the magnetization of the superparamagnetic Fe_3O_4 particles is parallel to B_{ext}. The stray field B_{stray} adds 0 – 200 mT to B_{ext} around the single domain particle. Figure 1d shows the dispersion relation of S1 and S2, including the additional stray field component for S1. As a result, the S1 EPR line broadens from about 500 µT for Fe/Fe_3O_4 nanocubes[16] to 36 mT for Fe_3O_4 octahedra (see below). Under these conditions, the red-shaded area indicates the S1 and S2 overlap at X-band frequencies and fulfills the population inversion and stimulated emission condition. This is experimentally confirmed by the power dependence of the S1 and S2 signals, as shown below.

Such molecules with population inversion under microwave excitation can be used for spin current detection. Signal S1 acts as a spin-current sensor.[10] The FMR-driven precession of the magnetization of the Fe_3O_4 particle injects a spin current into the paramagnetic center S1 at B_{res}. This spin torque transfer increases the population of the excited state, which affects the intensity of signal S2. In this way, we can detect spin current-induced changes with about one order of magnitude higher sensitivity as compared to the readout of S1.

2. METHODS

2.1 Synthesis of nanoparticles. Fe_3O_4-Au octahedral nanoparticles were obtained by thermal decomposition of $Fe(CO)_5$ and $HAuCl_4{\cdot}3H_2O$ in a high-temperature boiling solvent following a modified protocol initially described in References [14, 18, 19]. A mixture of 20 mL 1-octadecene, 2 mL (6 mmol) oleylamine, and 1.9 mL (6 mmol) oleic acid was heated to 120°C under argon flow and degassed for 30 minutes. Then, 0.3 mL (2 mmol) $Fe(CO)_5$ was injected. 3 minutes later, a mixture of freshly prepared and degassed 40 mg (0.1 mmol) $HAuCl_4{\cdot}3H_2O$, 0.5 mL (1.5 mmol) oleylamine, and 5 mL 1-octadecene was added, and the temperature was slowly increased (3.3°C/min) to 315°C. After 3 hours of reflux, the reaction mixture was cooled down to room temperature. During the synthesis, probes (aliquots ≈100 μL) were taken at different reaction mixture temperatures and reflux times at 315°C. In this way, we elucidated the nucleation, growth, and faceting towards an octahedral shape. The structural and magnetic properties of the nanoparticles have been published elsewhere.[18] The Au nanoparticle seeds allow for the growth of high-quality magnetite nanocrystals with octahedral shape[14]. Long reflux times lead to higher degrees of faceting.[19] In the present study, we have chosen the aliquot taken from the reaction mixture after 180 min reflux at 315°C. Figure 2 (a) and (b) present transmission electron microscopy (TEM) images of the Fe_3O_4 particles (discussion below).

2.2. Sample preparation. For the EPR/FMR investigations of the Fe_3O_4 particles and OA molecules on their surface acting as a spin current detector, we prepared several samples to optimize for reasonable coverage and avoid large agglomerates on a planar GaAs(100) substrate, which shows no resonant microwave absorption. We diluted the aliquot by factor 40 with 1-octadecene, and 10 μl of the resulting colloidal solution was deposited on a 4x4 mm^2 GaAs (100) substrate and dried in air. The SEM image in Figure 2 (c) shows a representative area of Fe_3O_4 particles on the GaAs(100). The particles distribute over the surface at sub-monolayer coverage.

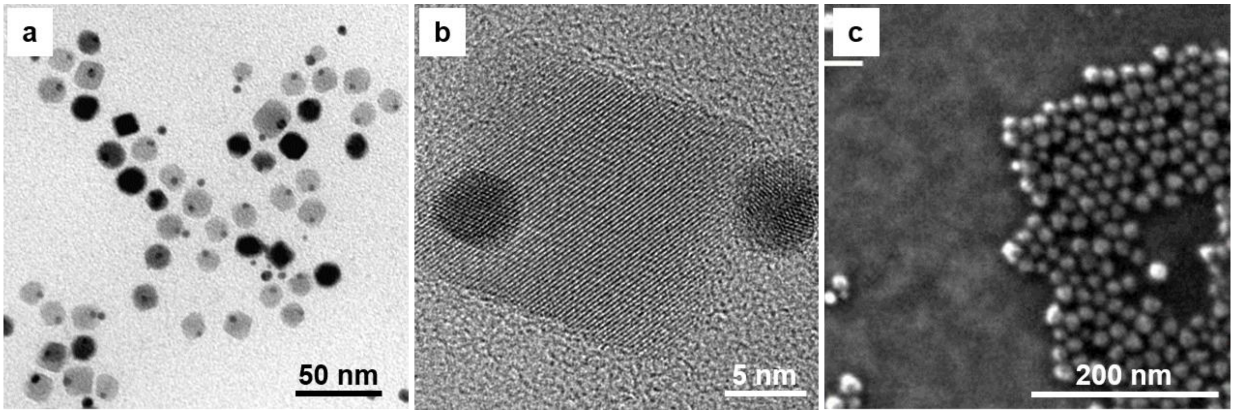

Figure 2. (a) TEM image of the Fe_3O_4-Au nanoparticles. (b) High-resolution TEM image of a single octahedral nanoparticle grown on an Au seed (dark contrast). The Au particle on the right is the seed of a neighboring Fe_3O_4 particle (not shown). (c) SEM image of the nanoparticles distributed on a GaAs(100) substrate for magnetic resonance measurements at sub-monolayer coverage.

2.3 EPR/FMR measurements. The angular-dependent magnetic resonance measurements were performed at a microwave frequency of f = 9.42 GHz using a conventional Bruker Elexsys E-500 X-band EPR spectrometer in fields up to 1.6 T at ambient temperature. The power-dependent EPR measurements were performed between 0.6 mW and 197 mW, the first being the lowest power at which the highly loaded cavity was still perfectly tunable, and the latter represents highest power of the Bruker microwave bridge. All spectra show the derivative of the microwave absorption using lock-in detection at field modulation of 100 kHz and amplitudes of 0.1 µT (EPR) or 0.2 mT (FMR).

2.4 Micromagnetic simulations. The effective field calculations of a model Fe_3O_4 particle were performed using the GPU-based software package mumax3.21.[20] The simulation grid consists of $320 \cdot 320 \cdot 120$ cells in x-y-z directions with the size of a single cell of $(0.2\ \text{nm})^3$. We used the simulation parameters for Fe_3O_4: saturation magnetization $M_{sat} = 4.85 \cdot 10^5$ A/m, exchange stiffness $A_{ex} = 1.32 \cdot 10^{-11}$ J/m and a first order cubic anisotropy constant $K_1 = -1.36 \cdot 10^4$ J/m^3. Values were taken from the literature.[21] For energy minimization, the built-in MuMax3 function "relax()" has been used. The static magnetic bias field was rotated around the x-y plane matrices starting at the +x-direction. The results were visualized using the Paraview software.[22]

3. RESULTS AND DISCUSSION

3.1 Fe_3O_4 nanoparticles for spin pumping experiments. For the present study, we have chosen ferrimagnetic Fe_3O_4 nanoparticles in their superparamagnetic state covered by OA. The particle size is 15.4 ± 2.2 nm Fe_3O_4 and 3.9 ± 0.9 nm Au.[18] During synthesis, the Au seeds crystallize first and improve the crystal quality of the Fe_3O_4 (see methods). Figure 2a,b present transmission electron microscopy (TEM) images at low and high resolution, respectively. The different projections of octahedra (rhombus, rectangle, and hexagon) can be identified in Figure 2a. Different contrasts of Fe_3O_4 nanocrystals arise from their individual crystallographic orientation with respect to the incident electron beam. The high-resolution TEM image in Figure 2b proves the single-crystalline structure of the Fe_3O_4 octahedra in the rectangular projection with edge lengths of about 19 nm and 15 nm, respectively. For the EPR/FMR investigations, we deposited the Fe_3O_4 particles coated by OA on a single-crystalline GaAs(100) substrate, which shows no resonant microwave absorption. The scanning electron microscopy (SEM) image in Figure 2c shows a representative area of Fe_3O_4 particles deposited on GaAs(100). The particles are distributed in planar clusters with sub-monolayer coverage.

3.2 Characterization of the ultrasensitive detection system. The molecular detection scheme reacts very sensitively to power variations of the resonant excitation. Figure 3a presents the experimental EPR spectra of S1 and S2. These have strongly different peak-to-peak linewidths of ΔB_{S1} = 36 mT and ΔB_{S2} = 0.11 mT, respectively. Note that while the width of S2 is given by its natural linewidth (lifetime 60 ns), the S1 linewidth is an envelope of the superposition of resonances with ΔB = 0.5 mT from individual nanoparticles resulting from the stray field distribution. Keep in mind that the overlap of S1 and S2 resonance lines is required for the population inversion of S2 states to achieve the stimulated emission. The octahedral-shaped nanoparticles provide the necessary local variation of the magnetic stray field. The micromagnetic simulations of the effective field (see Supporting Information Figures S2 and S3) quantify the shift of the S1 resonance position $h\nu = g\mu_B B_{eff}$ towards smaller fields and the increased linewidth. Minor differences with respect to the simulation (see Supplementary Figure S4) are due to dipolar interactions of adjacent particles not considered in the simulation.

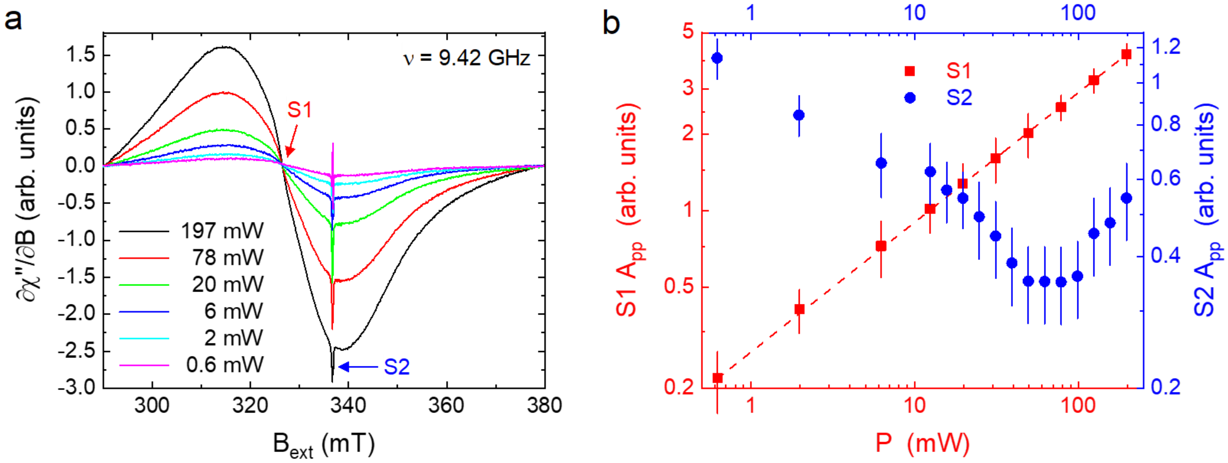

Figure 3. (a) EPR spectra of signals S1 and S2 for selected microwave power at ν = 9.42 GHz, modulation amplitude of 0.1 mT and 300 K. The ordinate is the derivative of the absorptive part of the high-frequency susceptibility with respect to B as function of B_{ext}. (b) Double logarithmic plot of the peak-to-peak amplitude A_{pp} of S1 (left) and S2 (right) as a function of microwave power. The dashed line is fit to the S1 A_{pp} at slope 0.51±0.01.

The paramagnetic center S2 results from partial radical formation during oxidation of OA by splitting a hydrogen atom next to the carbon double bond (cf. Figure 1a) during particle synthesis at 315 °C[18]. This is also observed when heating OA in nitrogen atmosphere besides the partial cis/trans isomerization[23] of OA (see Supplementary Information Chapter 2 and Figure S5). We estimate that S1 has about 250 times higher intensity as compared to S2. Thus, the number of S1 excitations shifted by the stray field to the position of the S2 resonance field is in the same order of magnitude, yielding the stimulated emission of S2 (cf. Figure 1d). Since the stray field at S2 is much larger than the resonance field ($B_{stray} >> \omega / \gamma$), a signal at the position of S2 can only occur via radiationless energy transfer from S1 to S2 within the same molecule. Consequently, the signal at S2 will react very sensitively to any change in the excitation of S1.

In Figure 3a, the S2 linewidth is 110 μT, which is 3 times smaller than in heated OA (Supplementary Figure S5). We explain this by the better-defined bond of OA to the Fe_3O_4 surface. The lifetime of signal S2 is 5 times longer than the one of S1 (linewidth 500-600 μT)[10]. Spin pumping is detected in the short-lived S1. In turn, S1 is also responsible for the population inversion between lower and higher energy spin states of S2 as detected by power-dependent (P) spectra from 0.62 mW to 197.12 mW (Figure 3b). The peak-to-peak amplitude S1 A_{pp} shows the expected standard $P^{0.5}$ dependence. On the other hand, S2 A_{pp} decreases with increasing power up to 80 mW, followed by a gradual increase above 100 mW. We explain these opposing trends by the strongly different lifetimes and number of contributing spins. Up to 80 mW, S1 pumps S2, and consequently, the population inversion shows up as a decreasing amplitude S2 A_{pp}. In other words, more spins relax from the excited state by stimulated emission than are excited by stimulated absorption. Further enhancement of microwave power above 100 mW additionally increases the stimulated emission. This leads to an increase in the reflected microwave power at the cavity, resulting in the increase in the detected intensity of S2 at high power values. The fine structure of the S2 signal is further discussed in the next section.

3.3 Spin pumping detection. Spin pumping is generated by collective resonant microwave excitation, which, for brevity, we call ferromagnetic resonance (FMR) of the superparamagnetic Fe_3O_4 nanoparticles. If the FMR overlaps with the EPR, spin torque, or analogously, spin currents are injected into OA molecules. In the in-plane configuration ($\theta = 88°$), the FMR line of the Fe_3O_4 octahedra is located at lower resonance fields (blue line in Figure 4b) and does not overlap with the EPR of S1 and S2. In this configuration, no spin pumping occurs. When the FMR resonance matches the EPR of OA by changing the polar angle θ between sample and external field, spin currents from Fe_3O_4 are injected. We call this orientation spin pumping configuration (SPC).[10] Figure 4a shows the polar angular-dependent magnetic resonance as an amplitude contour plot to identify the origin of the observed 3 distinct resonances. The modulation amplitude was set to 0.2 mT, pronouncing the broader resonance (FMR) for better visibility and partially suppressing S1 and S2 due to overmodulation. The FMR of the Fe_3O_4 shows uniaxial anisotropy with the hard direction in the out-of-plane configuration, as expected for the nanoparticles deposited on a flat substrate (cf. Figure 2c). The S1 and S2 EPR lines are independent of the polar angle. Figure 4b displays 3 spectra for selected angles as indicated by color-coded horizontal lines in the contour plot in Figure 4a. In the out-of-plane configuration ($\theta = 0°$) and in-plane configuration ($\theta = 88°$), S1 and S2 EPR lines are clearly separated from the Fe_3O_4 FMR line at $B_{res}^{FMR} = 480$ mT (green) and 250 mT (blue). The superposition of FMR and EPR signals is achieved at the intermediate angle $\theta = 46°$ (red). This is the SPC at which the 3 resonances (Fe_3O_4 FMR and OA S1/S2 EPR) overlap.

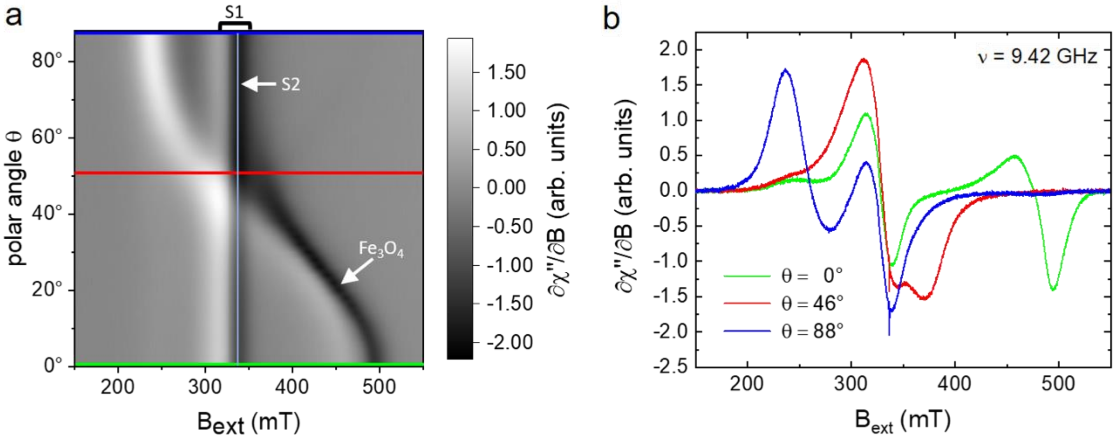

Figure 4. (a) Amplitude contour plot of the polar angular dependence of the magnetic resonance at 9.42 GHz, modulation amplitude of 0.2 mT, and 300 K. Fe_3O_4 FMR and S1/S2 EPR signals are indicated. Colored horizontal lines represent single spectra. (b) Absorption spectra at $\theta = 0°$ (out-of-plane), $\theta = 46°$ (spin-pumping configuration) and $\theta = 88°$ (in-plane configuration).

To analyze the effect of spin pumping from Fe_3O_4 nanoparticles into the paramagnetic molecules we compare the S1 and S2 signals in SPC to the one in in-plane configuration. Experimental spectra of 6 selected power values in SPC are shown in Figure 5a. Here, the field resolution (6 µT) and the modulation (0.1 mT) have been optimized for the EPR Signals S1 and S2. Due to the small field modulation, the intensity ratios of the FMR to the EPR lines change by about one order of magnitude. In Figure 5a, we show the EPR lines after subtraction of the Fe_3O_4 FMR line in SPC. Figure 5c shows several smaller resonances close to the S2 position, which all obey the $P^{0.5}$-dependence as expected for molecules in EPR. We ascribe these signals to excess OA molecules and OA bonded to the Au seeds (cf. Figure 2). The main signal, as indicated by the vertical dashed line in Figure 5c, shows a different trend. Its intensity decreases with increasing microwave power. Figures 5b and 5d present the peak-to-peak amplitudes of the EPR lines S1 and S2 as a function of microwave power in in-plane and SPC configurations in double logarithmic plots. The square root dependence holds for both S1 EPR signals in in-plane and SPC configurations. In SPC, however, S1 A_{pp} is reduced by almost a factor of 2. This reduced intensity when FMR and EPR signals are superimposed results from the spin current injection from the resonantly driven ferromagnet across the interface into S1, as explained before.[10] Excited FMR spins at the Fe_3O_4 surface contribute to the S1 excitation of OA molecules, and thus, less microwave power is needed to excite the same number of chemisorbed OA. In summary, the change in the power dependence of the S1 A_{pp} is a measure of the spin-pumping effect.

Figure 5d displays the peak-to-peak amplitude of signal S2 in SPC (black) and in-plane (red) configurations. As already discussed above, the S2 amplitude is decreasing with increasing power due to the larger population inversion. We detect a minimum of the S2 line intensity at 30 mW for SPC as compared to 80 mW for the in-plane configuration. Therefore, the effect is stronger in SPC than in-plane configuration. Due to the additional S1 EPR excitation by spin pumping from FMR, more S1 excited states are available leading to enhanced stimulated emission of S2, thus decreasing the absorption of externally fed microwaves.

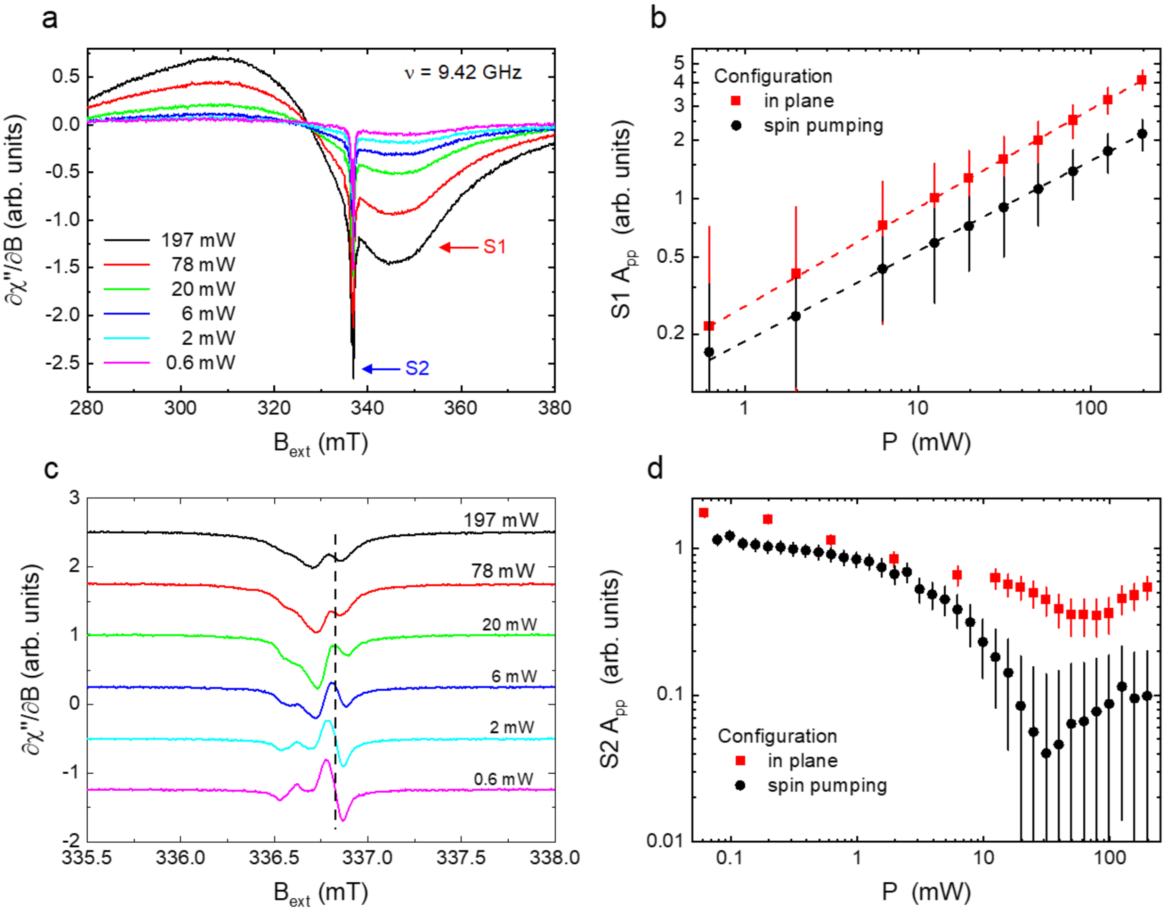

Figure 5. (a) EPR spectra of signals S1 and S2 in spin-pumping configuration at polar angle θ = 46° for selected microwave power at ν = 9.42 GHz, modulation amplitude of 0.1 mT and 300 K. (b) Peak-to-peak amplitude A_{pp} of S1 for in-plane and spin-pumping (SPC) configurations as function of microwave power in double logarithmic representation. The dashed lines are fits to S1 A_{pp} at slope 0.51±0.01 (in-plane) and 0.47±0.01 (spin-pumping). (c) Magnification of the S2 region in SPC from panel (a) after subtracting the Fe_3O_4 FMR and S1 EPR signals. (d) Peak-to-peak amplitude A_{pp} of S2 as indicated by the dashed line in panel (c) for in-plane and spin-pumping configuration as a function of microwave power in double logarithmic representation.

The S1 EPR signal has about 5 times shorter natural lifetime (broader linewidth) than S2 (sharper linewidth). The change of the dip-position from 80 mW to 30 mW in the power dependence of the reflected microwave intensity measures the increase of stimulated emission in the S2 signal. The dip positions in SPC and in-plane configurations indicate the stimulated emission. The shift of the dip position when using 50 mW is a direct measure of the spin current, i.e. the number of spins crossing the Fe_3O_4/OA interface.

4. CONCLUSIONS

We presented a novel detection scheme that can directly sense spin currents at ambient temperature at the molecular level. By exploiting signal S2 in oleic acid at the surface of Fe_3O_4 nanoparticles, the high sensitivity is gained, which is necessary to detect spin currents in polyhedral nanosystems. This new spin pumping detector eliminates the requirement of film-shaped samples, typically necessary for established contemporary techniques. With the demonstrated ability to study nanoscale particle ensembles, one can envision this sensing technique for spin transistor applications[24], incorporating thousands to millions of nanostructures components. In conclusion, using organic molecules as a sensor may open a path to connecting to molecular spintronics. Our stimulated emission-based detection scheme is a broadly applicable, non-invasive technique for the direct and remote measurement of spin currents without electrical contacts. This concept can be further developed into an enhanced quantum sensor[25,26], e.g. for molecular spintronics, which bridges magnetism and molecular electronics on atomic level, e.g. for applications in organic spintronics and quantum computing[27].

ASSOCIATED CONTENT

Supporting information

The Supporting Information contains four sections with figures as indicated in the sections below.

1. Origin of EPR line distribution of the S1 EPR signal

   Figure S1. Cross section of the effective field distribution (B_{eff}).

   Figure S2. Lateral distribution of the effective field for various external fields.

   Figure S3. Lateral distribution of the effective field for $B_{ext} = 285$ mT.

   Figure S4. Gathered area from simulations where $B_{res}^{S1} = B_{ext} + B_{stray} = 341 \pm 1$ mT is fulfilled near the Fe_3O_4 nanoparticle surface.

2. Origin of the S2 EPR signal

   Figure S5. EPR signal of pure liquid OA in a glass tube before and after 1 h of heating at 640 K.

   Figure S6. (a) Amplitude contour plot of the power dependence of the EPR signal of pure OA. (b) Double logarithmic plot of the peak-to-peak amplitude A_{pp} of OA as function of microwave power.

3. Information on supplementary video files

   Video-S1. Image series from micromagnetic simulations for B_{ext} = 150 mT, 285 mT, and 400 mT showing the lateral distribution of cells obeying B_{eff} = 341±1 mT (red) from the center (001) plane of the nanoparticle towards the upper surface with 0.2 nm (cell size) steps.

   Video-S2. Image series from micromagnetic simulations for B_{ext} = 285 mT and rotating magnetic field direction in the x-y plane in 5° steps around the particle using Euler rotation matrices starting at the positive x-direction [100] direction and ending towards y-direction as indicated by the coordinates. For all 3 planes (and the planes in between) many cells close to the particle surface show B_{eff} = 341 ± 1 mT for all orientations of B_{ext} as indicated by the red color.
4. References

Video files

The Supplementary Figures S2 and S3 are animated GIF images. In case the reader's pdf viewer does not support animated images, the corresponding video files Video-S1 and Video-S2 can also be found as additional material for download.

Author contributions

Experiments were designed by R.M., M.F., and U.W. M.V.E. synthesized and characterized the nanoparticles. T.S. R.M. and U.W. prepared the samples, performed the measurements, and analyzed the data. T.S., R.M., M.F., M.V.E., and U.W. discussed the data. T.F., R.M., and U.W. performed the theoretical calculations and evaluated the simulations. T.F., R.M., M.F., and U.W. co-wrote the manuscript with input from all co-authors.

Funding sources

This work is in part funded by the Deutsche Forschungsgemeinschaft (DFG, German Research Foundation) – Project-ID 405553726 within CRC/TRR 270, projects A04 and B02. T.F. and T.S. thank the German Research Foundation (DFG projects OL513/1-1 and SE2853/1-1) for financial support. T.F. acknowledges Lawrence Berkeley National Laboratory for funding through LDRD Award: Development of a Continuous Photon Counting Scheme for Time Resolved Studies.

Notes

The authors declare no competing financial interest. The datasets used and/or analyzed during the current study are available from the corresponding author on reasonable request.

ACKNOWLEDGEMENTS

We thank T. Marzi for the experimental work at the early stage of the study. B. Zingsem, D. Spoddig, and M. Spasova are acknowledged for fruitful discussions. We thank Y. A. Nalench and M. A. Abakumov for supporting the synthesis and characterization of the nanoparticles.

REFERENCES

1. Denning, P. J.; Lewis, T. G., Exponential Laws of Computing Growth. *Communications of the Acm* **2017**, *60*, 54-65.
2. Wolf, S. A.; Chtchelkanova, A. Y.; Treger, D. M., Spintronics - A Retrospective and Perspective. *IBM Journal of Research and Development* **2006**, *50*, 101-110.
3. Wolf, S. A.; Awschalom, D. D.; Buhrman, R. A.; Daughton, J. M.; von Molnár, S.; Roukes, M. L.; Chtchelkanova, A. Y.; Treger, D. M., Spintronics: A Spin-Based Electronics Vision for the Future. *Science* **2001**, *294*, 1488-1495.
4. Žutić, I.; Fabian, J.; Das Sarma, S., Spintronics: Fundamentals and Applications. *Reviews of Modern Physics* **2004**, *76*, 323-410.
5. Hoffmann, A.; Bader, S. D., Opportunities at the Frontiers of Spintronics. *Physical Review Applied* **2015**, *4*, 047001.
6. Saitoh, E.; Ueda, M.; Miyajima, H.; Tatara, G., Conversion of Spin Current into Charge Current at Room Temperature: Inverse Spin-Hall Effect. *Applied Physics Letters* **2006**, *88*, 182509.

7. Sinova, J.; Valenzuela, S. O.; Wunderlich, J.; Back, C. H.; Jungwirth, T., Spin Hall Effects. *Reviews of Modern Physics* **2015**, *87*, 1213-1259.

8. Hait, S.; Husain, S.; Bangar, H.; Pandey, L.; Barwal, V.; Kumar, N.; Gupta, N. K.; Mishra, V.; Sharma, N.; Gupta, P.; Yadav, B. S.; Muduli, P. K.; Chaudhary, S., Spin Pumping Through Different Spin-Orbit Coupling Interfaces in β-W/Interlayer/Co_2FeAl Heterostructures. *ACS Applied Materials & Interfaces* **2022**, *14*, 37182-37191.

9. Zhang, J. Y.; Zhao, Y. C.; Dou, P. W.; Peng, W. L.; Huang, H.; Deng, X.; Wang, Y. B.; Liu, J. L.; Xu, J. W.; Zhu, T.; Qi, J.; Zheng, X. Q.; Wu, Y. F.; Shen, B. G.; Wang, S. G., Controllable Spin-Orbit Torque Induced by Interfacial Ion Absorption in Ta/CoFeB/MgO Multilayers with Canted Magnetizations. *ACS Applied Materials & Interfaces* **2023**, 15 (42), 49902–49910.

10. Marzi, T.; Meckenstock, R.; Masur, S.; Farle, M., Spin-Current Detection via an Interfacial Molecular Paramagnet. *Physical Review Applied* 2018, *10,* 054002.

11. Mollier, J. C.; Hardin, J.; Uebersfe.J, Theoretical and Experimental Sensitivities of ESR Spectrometers Using Maser Techniques. *Review of Scientific Instruments* **1973,** *44*, 1763-1771.

12. Elitzur, M., Astronomical Masers. *Annual Review of Astronomy and Astrophysics* **1992**, *30*, 75-112.

13. Claussen, M., Astronomical Masers. *Science* **2004**, *306*, 235-236.

14. Efremova, M., V; Nalench, Y. A.; Myrovali, E.; Garanina, A. S.; Grebennikov, I. S.; Gifer, P. K.; Abakumov, M. A.; Spasova, M.; Angelakeris, M.; Savchenko, A. G.; Farle, M.; Klyachko, N. L.; Majouga, A. G.; Wiedwald, U., Size-Selected Fe_3O_4 Au Hybrid Nanoparticles for Improved Magnetism-based Theranostics. *Beilstein Journal of Nanotechnology* **2018**, *9*, 2684-2699.

15. Antoniak, C.; Lindner, J.; Spasova, M.; Sudfeld, D.; Acet, M.; Farle, M.; Fauth, K.; Wiedwald, U.; Boyen, H. G.; Ziemann, P.; Wilhelm, F.; Rogalev, A.; Sun, S., Enhanced Orbital Magnetism in $Fe_{50}Pt_{50}$ Nanoparticles. *Physical Review Letters* **2006**, *97* (11), 117201.

16. Masur, S.; Zingsem, B.; Marzi, T.; Meckenstock, R.; Farle, M., Characterization of the Oleic Acid/Iron Oxide Nanoparticle Interface by Magnetic Resonance. *J. Magn. Magn. Mater.* **2016**, *415*, 8-12.

17. Poole, C., *Electron Spin Resonance*. Interscience Publishers John Wiley and Sons: 1967.
18. Nalench, Y. A.; Shchetinin, I. V.; Skorikov, A. S.; Mogilnikov, P. S.; Farle, M.; Savchenko, A. G.; Majouga, A. G.; Abakumov, M. A.; Wiedwald, U., Unravelling the Nucleation, Growth, and Faceting of Magnetite-Gold Nanohybrids. *Journal of Materials Chemistry B* **2020**, *8*, 3886-3895.
19. Efremova, M. V. *et al.* Magnetite-Gold Nanohybrids as Ideal All-in-One Platforms for Theranostics. *Scientific Reports* **2018**, *8*, 11295-11295.
20. Vansteenkiste, A. *et al.* The Design and Verification of MuMax3. *AIP Advances* **2014**, *4*, 107133.
21. Wu, H.-C., Arora, S. K., Mryasov, O. N. & Shvets, I. V. Antiferromagnetic Interlayer Exchange Coupling Between Fe_3O_4 Layers Across a Nonmagnetic MgO Dielectric Layer. *Applied Physics Letters* **2008**, *92*, 182502.
22. Ahrens, J. P. G., B.; Law, C. in *The Visualization Handbook* (ed. C.D. Hansen and C.R. Johnson) (Elsevier, 2005).
23. N. Cheng, J. Zhang, J. Yin, S. Li, *Heliyon* **2018**, 4, e00768.
24. W. Zhu, H. Lin, F. Yan, C. Hu, Z. Wang, L. Zhao, Y. Deng, Z. R. Kudrynskyi, T. Zhou, Z. D. Kovalyuk, Y. Zheng, A. Patanè, I. Žutić, S. Li, H. Zheng, K. Wang, Large Tunneling Magnetoresistance in van der Waals Ferromagnet/Semiconductor Heterojunctions. *Adv. Mater.* **2021**, 33, 2104658.
25. Wu, H.; Yang, S.; Oxborrow, M.; Jiang, M.; Zhao, Q.; Budker, D.; Zhang, B.; Du, J., Enhanced Quantum Sensing with Room-Temperature Solid-State Masers. *Science Advances* **2022,** *8*, eade1613.
26. Hahl, F. A.; Lindner, L.; Vidal, X.; Luo, T.; Oshima, T.; Onoda, S.; Ishil, S.; Zaitsev, A. M.; Capelli, M.; Gibson, B. C.; Grentree, A. D.; Jeske, J., Magnetic-Field-Dependent Stimulated Emission from Nitrogen-Vacancy Centers in Diamond. *Science Advances* **2022**, *8*, eabn7192.
27. Cornia, A.; Seneor, P., Spintronics: The Molecular Way. *Nat Mater* **2017**, *16* (5), 505-506.

Graphical abstract